Free-Space Remote Sensing of Rotation at the Photon-Counting Level

Wuhong Zhang,[1] Jingsong Gao,[1] Dongkai Zhang,[1] Yilin He,[1] Tianzhe Xu,[1] Robert Fickler,[2,*] and Lixiang Chen[1,†]

[1] *Department of Physics, Jiujiang Research Institute and Collaborative Innovation Center for Optoelectronic Semiconductors and Efficient Devices, Xiamen University, Xiamen 361005, China*

[2] *Department of Physics, University of Ottawa, 25 Templeton St., Ottawa, Ontario K1N 6N5, Canada*

(Received 3 June 2017; revised manuscript received 11 June 2018; published 4 October 2018)

The rotational Doppler effect associated with light's orbital angular momentum has been found to be a powerful tool to detect rotating bodies. However, this method has only been demonstrated experimentally on the laboratory scale under well-controlled conditions so far. However, its real potential lies in practical applications in the field of remote sensing. We establish a 120-m-long free-space link between the rooftops of two buildings and show that both the rotation speed and the rotational symmetry of objects can be identified from the detected rotational Doppler frequency shift signal at photon-count level. Effects of possible slight misalignments and atmospheric turbulence are quantitatively analyzed in terms of mode power spreading to the adjacent modes as well as the transfer of rotational frequency shifts. Moreover, our results demonstrate that with the preknowledge of the object's rotational symmetry one may always deduce the rotation speed no matter how strong the coupling to neighboring modes is. Without any information of the rotating object, the deduction of the object's symmetry and rotational speed may still be obtained as long as the mode-spreading ratio does not exceed 100%. Our work supports the feasibility of a practical sensor to remotely detect both the speed and symmetry of rotating bodies.

DOI: 10.1103/PhysRevApplied.10.044014

I. INTRODUCTION

The Doppler effect is a well-known phenomenon describing the frequency shift of a wave, such as sound waves and light waves. The frequency emitted by a moving source becomes higher as the source is approaching an observer, while it becomes lower as it is receding. This linear Doppler effect is widely used for sonar and radar systems to deduce the speed of a moving object [1]. In contrast to linear motion, a rarely encountered example is the angular version of the Doppler shift arising from rotation [2]. The rotational Doppler effect was first observed by Garetz and Arnold, who used rotating half-wave plates of angular velocity Ω to imprint a frequency shift 2Ω to circularly polarized light [3]. Such a frequency shift is, in essence, associated with the spin angular momentum of photons, and can be understood from the dynamically evolving geometric phase in the light of the Poincare sphere [4]. More recently, the rotational Doppler effect was also verified in the second-harmonic generation with a spinning nonlinear crystal of threefold rotational symmetry [5]. In addition to spin, a light beam with a twisted phase front of $\exp(i\ell\phi)$ carries $\ell\hbar$ orbital angular momentum (OAM) per photon, where ϕ is the azimuthal angle and ℓ is an integer [6]. It was first demonstrated by Courtial *et al.* that a rotating Dove prism could impart the OAM beams with a frequency shift of $\ell\Omega$, where Ω denotes the angular velocity [7,8]. Via the coherent interaction of OAM beams with atom samples, Barreiro *et al.* reported on the first spectroscopic observation of rotational Doppler shift [9]. Also, Korech *et al.* developed an intuitive method to observe the molecular spinning based on the rotational Doppler effect [10].

Recently, considerable attention has been paid to exploit the twisted light's rotational Doppler effect to detect rotating bodies. Lavery *et al.* demonstrated that the angular speed can be deduced by detecting the frequency shift of on-axis OAM components that are scattered from a spinning object with an optically rough surface [11]. They further employed an OAM-carrying white-light beam and only observed a single frequency shift within the same detection mode [12]. Rosales-Guzmn *et al.* showed that under different OAM-mode illuminations, the full three-dimensional movement of particles could be characterized by using both the translational and rotational Doppler effect [13]. Fang *et al.* experimentally demonstrated that both the rotational and linear Doppler effect actually share a common origin such that one can use one effect to drive the other effect [14]. Zhao *et al.* extended the OAM illumination beam into the radio-frequency area and detected the speed of a rotor in a proof-of-concept experiment [15]. Based on the rotational Doppler effect, Zhou *et al.* devised

*robertfickler@web.de
†chenlx@xmu.edu.cn

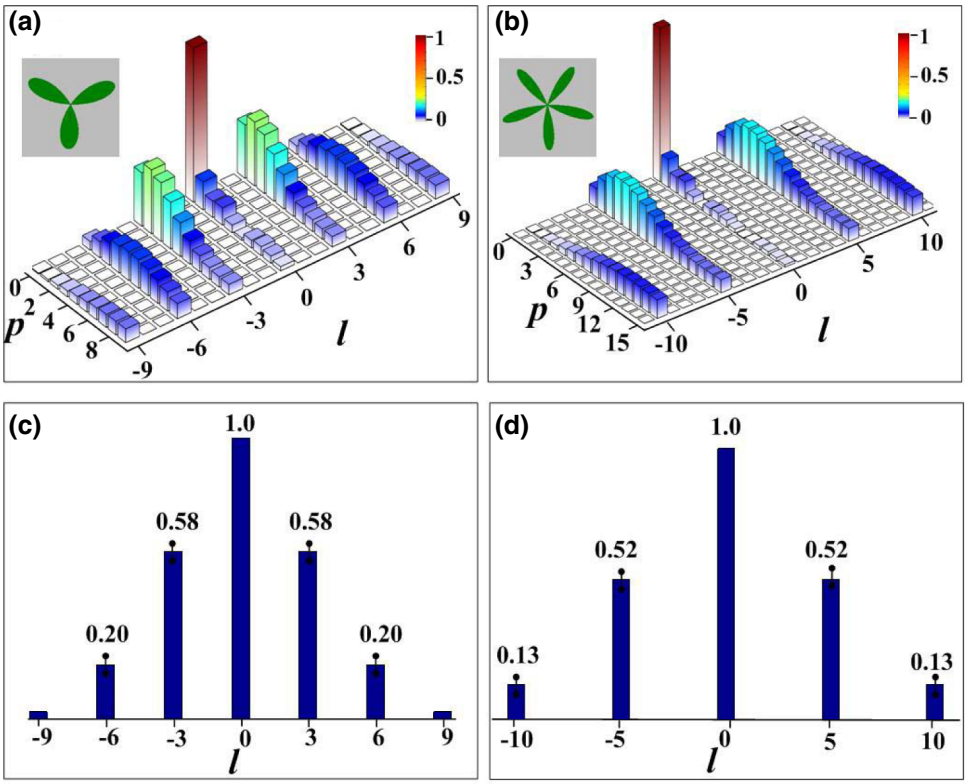

FIG. 1. Spiral spectrum of the image gives an intuitive indication of the object symmetry. The top panel is the peak-normalized LG mode spectra while the bottom panel is the pure-OAM spectra. (a),(c) A three-leaf clover. (b),(d) A five-petal pentas.

an OAM-spectrum analyzer that enables simultaneous measurements of the power and phase distributions of OAM modes [16]. Although the real potential of the rotational Doppler effect lies in its practical application in noncontact remote sensing [17,18], we note that thus far no experimental verification of the rotational Doppler effect has been conducted outside of the laboratory.

The challenges for a long-distance implementation originate from the OAM-mode spreading induced by atmospheric turbulence and the low-photon collection efficiency due to beam-divergence misalignment [19]. Here we report observation of the rotational Doppler effect over a 120-m free-space link between the rooftops of two buildings across the Haiyun Campus of Xiamen University in a city environment. Our scheme works with extremely weak-light illumination by employing a single-photon-counting module. This work moves a step towards remote-sensing applications in a realistic environment with twisted light's rotational Doppler effect.

II. THEORETICAL ANALYSIS AND SIMULATIONS

We assume that the rotating object is mathematically described by a complex function $\psi(r,\varphi)$ in the cylindrical coordinates and is illuminated with a fundamental Gaussian mode. As the Laguerre-Gaussian (LG) modes form a complete and orthogonal basis, we can describe the light field reflected from the object as $\psi(r,\varphi) = \sum_{\ell,p} A_{\ell,p}\mathrm{LG}_p^{\ell}(r,\varphi)$, where $\mathrm{LG}_p^{\ell}(r,\varphi)$ denotes the LG mode with azimuthal and radial indices ℓ and p, respectively, and $A_{\ell,p} = \int\int [\mathrm{LG}_p^{\ell}(r,\varphi)]^{*}\psi(r,\varphi)rdrd\varphi$ is the overlap amplitude. The method of using a coherent superposition of LG modes to represent an object was called digital spiral imaging by Torner *et al.* [20], and has been found as an effective technique to encode optical information and retrieve topographic information of an object, which is particularly useful for objects of high spatial symmetry [21,22]. We plot the LG mode spectra, $|A_{\ell,p}|$, for two typical objects, i.e., a three-leaf clover and a five-petal pentas in Fig. 1. One can see from the top panel of Fig. 1, the dominant LG modes are those with the azimuthal indices of $\ell = 0, \pm 3, \pm 6, \ldots$ [Fig. 1(a)] and $\ell = 0, \pm 5, \pm 10, \ldots$ [Fig. 1(b)], being associated with the threefold and fivefold rotational symmetry of the clover and pentas, respectively. This symmetry can be illustrated more evidently by the pure-OAM spectra characterized by $P_{\ell} = \sum_p |A_{\ell,p}|^2$, as a sum of the mode weights over the radial p index. In the lower panel of Fig. 1, we plot the pure-OAM spectra for the three-leaf clover [Fig. 1(c)] and five-petal pentas [Fig. 1(d)]. This follows the experimental expectation more closely, because our detection technique uses a pure-phase grating that only distinguishes between different ℓ modes irrespective of their radial structure. More details of the mode expansion can be found in our recent paper [23].

The framework of digital spiral imaging provides an intuitive understanding of the mechanism of the rotational

Doppler effect. If the object is rotated by a constant angular speed Ω around its own axis, a time-varying phase shift of $\ell\Omega t$ will be imparted to each OAM eigenmode. As a consequence, we rewrite the transmitted or reflected light fields as

$$\psi(r,\varphi,t) = \sum_{\ell,p} A_{\ell,p} \mathrm{LG}_p^{\ell}(r,\varphi)\exp(i\ell\Omega t), \qquad (1)$$

which manifests the OAM-dependent frequency shift $\ell\Omega$. By using specific OAM superposition modes $\Phi(r,\varphi) = [\exp(i\ell\phi) + \exp(-i\ell\phi)]/\sqrt{2}$ to detect the reflected light fields, we can obtain the signal as

$$I(t) = \left| \int\int \Phi^*(r,\varphi)\psi(r,\varphi,t) r dr d\Phi \right|^2 \propto 2P_\ell[\cos(2\ell\Omega t) + 1] \qquad (2)$$

assuming $P_\ell = P_{-\ell}$. Hence, we find an intensity modulation of frequency $f_{\mathrm{mod}} = |2\ell\Omega|/2\pi$ for the detected superposition modes $\Phi(r,\varphi)$, and the signal intensity for this frequency component is just determined by P_ℓ. It is obvious that one cannot detect the intensity modulation signal with the OAM-mode spectrum $|P_\ell| = 0$. By analyzing the signal intensity of the entire OAM spectrum after FFT, the rotational symmetry of the object could also be inferred. Generally, as all of the constituent LG modes in Eq. (1) propagate individually in free space without coupling with each other, the mode weights $A_{\ell,p}$, i.e., the OAM spectra, will remain unchanged without any influence by atmospheric disturbance [24]. This indicates that the measurement of rotational Doppler effect f_{mod} at the distant receiver will be equivalent to that at the transmitter.

III. EXPERIMENTAL SETUP

We implement the 120-m free-space link between the rooftops of two buildings. Fig. 2 shows the transmitter and receiver locations. At the transmitter (top-left inset in Fig. 2), the fundamental Gaussian mode from a 633-nm helium-neon (He-Ne) laser beam (Thorlabs HNL210L), after being collimated by the first telescope, illuminates a computer-controlled spatial light modulator (SLM). We prepare the desired holographic gratings with the SLM to mimic the rotating objects, e.g., a clover and a pentas. The first diffraction order, which is selected by a 4-f filtering system ($f_1 = 500$ mm, $f_2 = 150$ mm), then acquires the profile of the rotating objects. The beam diameter on the image plane is about 2 mm, which is the diffraction-limited input beam diameter of the second telescope (Thorlabs GBE20-A). The telescope is used to further expand the beam to a diameter of about 40 mm, and is followed by the transmission of the rotating pattern over the 120-m free-space link to the receiver. Due to the diffraction of the image, we obtain a beam diameter of about 50 mm at the receiver. There, another 4-f filtering system with

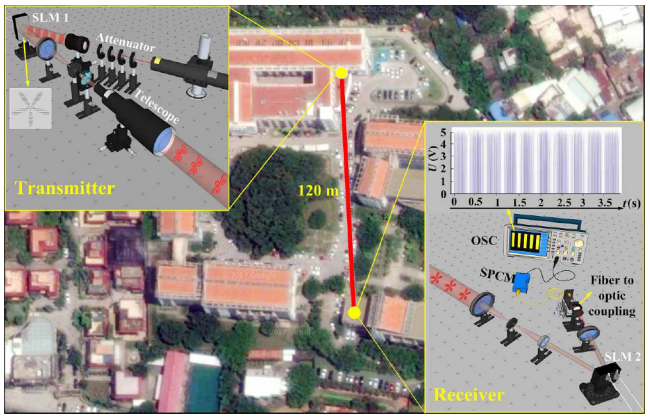

FIG. 2. 120-m free-space optical link implemented from building-to-building in the Haiyun Campus of Xiamen University. Left-top inset, optical setup of the transmitting terminal; right-bottom inset, optical setup of the receiving terminal. SLM, spatial light modulator; OSC, oscilloscope; SPCM, single-photon-counting module.

a collection lens of 100 mm in diameter ($f_3 = 500$ mm) and a reimaging lens ($f_4 = 75$ mm) is used to demagnify the collected beam to have a diameter of approximately 7.5 mm. Considering the limited aperture of the lens, we estimate that approximately 95% of the incoming light is collected to illuminate the second SLM. A holographic grating with desired superposition of $\pm\ell'$ OAM modes is displayed on another SLM and together with a third 4-f filtering system is used to select the first diffraction order and image the SLM plane on the single-mode fiber. The grating is used to convert the beam's wavefront to a plane wave, which could then be coupled efficiently into the single-mode fiber. This configuration acts as a mode filter, by which we measure the overlap probability, as described by Eq. (2).

In the experiment, we start by using the full power of the He-Ne laser with 21 mW to align the whole optical path. Then, we use a series of neutral-density filters to attenuate the laser beam to a very faint level and demonstrate the ability of our scheme to work at the photon-counting level. We employ the single-photon-counting module (SPCM, Excelitas) to detect single photons that are phase flattened and coupled into the single-mode fiber. The single-photon events are monitored by a Digital Phosphor Oscilloscope (DPO3012, Tektronix) over the measurement time of a few minutes. An example of a measured data set of single-photon detections can be seen in the right-bottom inset of Fig. 2. Along the time axis, each blue line represents an individual detection of a single-photon event. Thus the sparsity of the blue lines determines the numbers of single-photon events, i.e., more intensive lines correspond to more single-photon events. By subsequently applying a FFT to the time-varying photon-count sequence (approximately 10^6 single-photon events detected in each

measurement), we extract directly the frequency components. It is noted that the optical alignment between the receiver and transmitter is very important, as both lateral displacement and angular deflection could cause severe modal crosstalk [25,26]. To minimize possible misalignments, we couple a second He-Ne laser at the receiver into the fiber before each measurement and send the light back to the transmitter to make sure the forward and backward propagating beams are well overlapped at both stations. Moreover, to minimize vibrations induced by people walking around in the building of the sender, we perform all experiments after midnight.

IV. EXPERIMENTAL RESULTS

We first investigate the propagation features of the clover and pentas images transmitted through the 120-m free-space link. We use a low-noise electron multiplier CCD camera (EMCCD, E2V, 768 × 576 pixels) to record the light fields at both the transmitter and receiver. Figures 3(a) and 3(b) display false color images of the clover and pentas at the transmitter, respectively. One can see the intensity distribution has a little asymmetry due to the slight misalignment between the laser and grating on the SLM possibly induced by slight oblique incidence approximately 8°. Because of such an intensity asymmetry and the free-space diffraction, we can see from Figs. 3(c) and 3(d) that both the clover and pentas images become barely recognizable after propagating through the free-space link. We estimate that the photon flux recorded in each of these images is approximately 10^5 s^{-1} based on the sender power of the light field. At the receiver, we use holographic gratings for measuring specific OAM superposition, with diffraction efficiency approximately 20%. The fiber-optic coupling efficiency is approximately 80% and the SPCM detection efficiency is approximately 60% at 633 nm. Thus we record approximately 10^3 s^{-1} single-photon events.

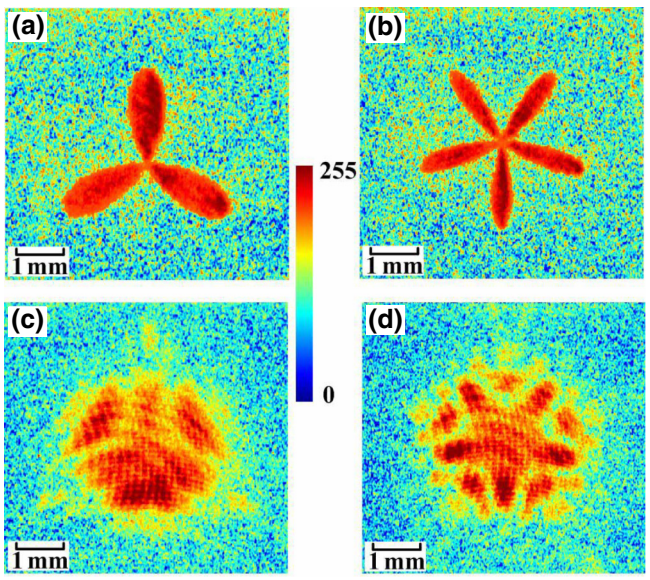

FIG. 3. Weak-light images of the rotating objects. (a),(b) Gray scale images of the clover and pentas recorded by an EMCCD camera at the transmitter, respectively. (c),(d) False color images of the clover and pentas images at the receiver, respectively.

Without losing generality, we restrict our first set of measurements to the clover and pentas with a rotating velocity $\Omega_1 = 91^\circ$ s^{-1} corresponding to a rotational frequency of 0.2528 Hz. According to Eq. (2), we measure OAM superspositions ranging from $\ell' = \pm 1$ to $\ell' = \pm 7$ for clover and up to $\ell' = \pm 11$ for pentas, respectively. After applying a FFT directly to the time-varying single-photon events, we obtain the experimental results in Fig. 4. The peak power frequency observed at $\ell' = \pm 3$ with $f = 1.526$ Hz and $\ell' = \pm 6$ with $f = 3.052$ Hz for the clover in Fig. 4(a), while at $\ell' = \pm 5$ with $f = 2.527$ Hz and $\ell' = \pm 10$ with $f = 5.102$ Hz for the pentas in Fig. 4(b), which manifests the threefold and fivefold rotational symmetry of the clover and pentas. We use a Gaussian-fitting curve and then calculate the width σ of each signal peak (here σ corresponds to $1/e$ of the maximum), which just characterizes the uncertainty of the experimental data. According to $f_{\mathrm{mod}} = |2\ell\Omega|/2\pi$, we deduce the rotating velocity with $\Omega_{\mathrm{clover}} = (91.44^\circ \pm 1.4^\circ)$ s^{-1} and $\Omega_{\mathrm{pentas}} = (90.97^\circ \pm 0.97^\circ)$ s^{-1}. We further set both the clover and pentas to rotate at $\Omega_2 = 136.5^\circ$ s^{-1} degree/s, corresponding to a rotational frequency of 0.3792 Hz to test our setup. From the measured power spectra in Fig. 5, we also find the peak frequency as labeled in red text. The analog data processing gives the deduced rotating velocity $\Omega_{\mathrm{clover}} = (137.34^\circ \pm 1.32^\circ)$ s^{-1} and $\Omega_{\mathrm{pentas}} = (137.34^\circ \pm 1.18^\circ)$ s^{-1}. The obtained results of rotation speed have a max error of about 0.6% (under laboratory condition, e.g., in [15], a max error of 0.36% was achieved without using a single-photon detector), which shows the good accuracy of our 120-m free-space rotation sensing at photon-counting level. Moreover, in the absence of any information about the detected rotation object, the peak power of the detected OAM frequency spectrum also provides a way to analyze the objects' rotational symmetry.

In addition to the expected signal from the rotating pattern, we also observe the frequencies $f = 3.052$ Hz, 4.578 Hz in the main mode $\ell' = \pm 3$ for the clover and $f = 5.102$ Hz, 7.629 Hz in $\ell' = \pm 5$ for the pentas under a rotation speed $\Omega_1 = 91^\circ$ s^{-1}, as denoted by the blue text in Figs. 4(a) and 4(b). Similarly, in Figs. 5(a) and 5(b), the same effect can also be observed. According to Eq. (2), the density distribution of photon counts over time should appear like a sinusoidal oscillation with $\ell' = \pm 3$ and $\ell' = \pm 5$, and the corresponding Fourier transform should only give one peak. However, in our practical detection the signal is obtained over a few minutes. Over that time frame, any slight misalignment caused by tiny vibrations of the

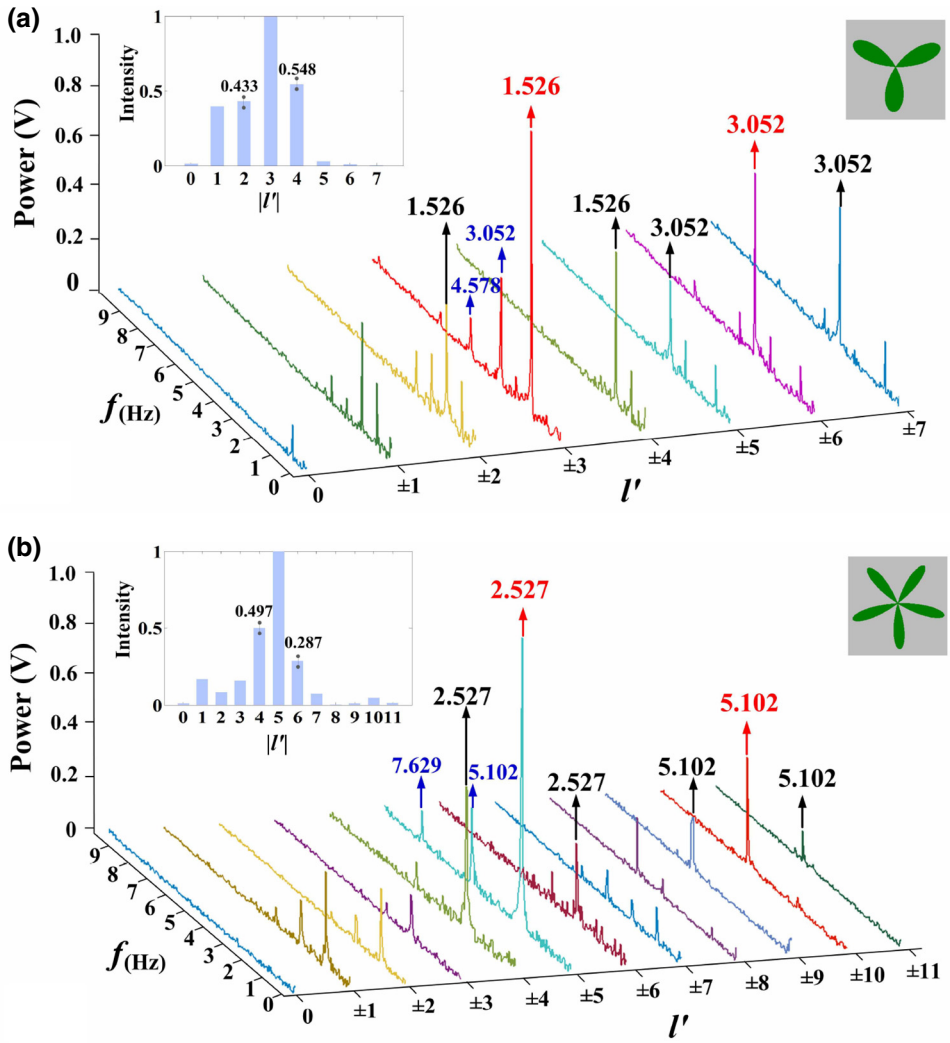

FIG. 4. Measured power spectra of rotational Doppler shifts. (a) Clover. (b) Pentas. Both are set to rotate at the same angular rate $\Omega_1 = 91^\circ\ s^{-1}$. The value of the frequency labeled in red text denotes the frequency of the main modes that are used to deduce the rotation speed. The frequency shifts denoted by black digits are undesired shifts that are mainly caused by mode crosstalk due to slight misalignment. Frequency shifts denoted by blue digits are additional shifts that might be caused by the recoded photon counts vs time that deviates from the sinusoidal manner. The inset bar graph shows the special frequencies (i.e., 1.526 Hz for clover and 2.527 Hz for pentas) for the different ℓ modes.

transmitter, leads to a deviation from the expected sinusoidal recording. Such slight deviations from the standard sinusoid of the photon-count density will cause higher harmonic peaks of frequency shifts when performing FFT.

As mentioned before, we should observe no modulation of the counts, i.e., $f = 0$ for those OAM modes with $|P_\ell| = 0$ as the simulation results in Figs. 1(c) and 1(d). However, in contrast to this theoretical expectation, we also observe the same frequency as the main modes, as labeled by the black text in Figs. 4 and 5. For example, for the different rotation frequency, we have $f = 1.526$ Hz, $f = 2.289$ Hz in the adjacent modes with $\ell' = \pm 2, \pm 4$ of the clover object, and $f = 2.527$ Hz, $f = 3.815$ Hz in modes $\ell' = \pm 4, \pm 6$ of the pentas object. We attribute this effect to energy spreading accompanied with the transfer of frequency shifts from the dominant modes to the adjacent ones. To show this effect more clearly, a bar graph of the amplitudes of the dominant frequencies ($\ell' = \pm 3$ for clover, $\ell' = \pm 5$ for pentas) are plotted as insets in each figure. There are about 49%, 30% mode spreading for clover and 39%, 48% for pentas. If we have preknowledge of an object's symmetry, this could be identified as erroneous measured frequency shifts such that the rotation speed will still be simply deduced from the dominant modes. However, if there is no information about the object, one needs to measure different OAM components ℓ' and deduce the symmetry from the measured spectrum to determine the dominant mode. In this case, if we measure ℓ', it is possible to obtain a mixing of frequency shifts from different OAM modes $\Delta\omega = \{2\ell'_1\omega, 2\ell'_2\omega, 2\ell'_3\omega, \ldots\}$. One reasonable assumption might be that with an energy spread to adjacent modes of more than 100%, a correct discrimination of the main mode is not easily possible anymore, such that the real frequency shifts and the symmetry of the object cannot be accurately deduced. Hence, the main contributions to the mode-spreading phenomenon will be carefully analyzed in the following paragraphs.

V. DISCUSSION

Firstly, it might be caused by slight misalignments between the receiving optical patterns and the holographic

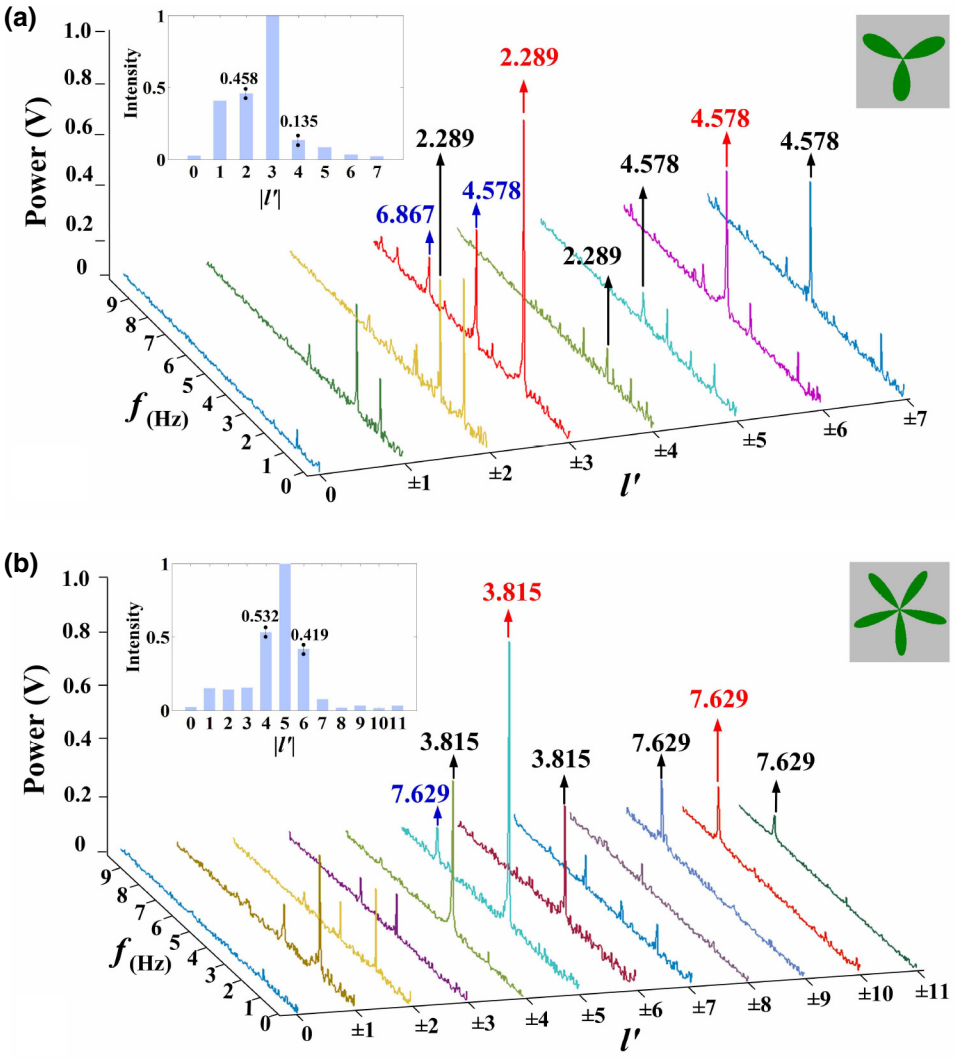

FIG. 5. Measured power spectra of rotational Doppler shifts. (a) Clover. (b) Pentas. Both are set to rotate at the same angular rate $\Omega_2 = 136.5^\circ\ \mathrm{s}^{-1}$. Different colors are used for the same purpose as described in the caption of Fig. 4. The inset bar graph shows the special frequencies (i.e., 2.289 Hz for clover and 3.815 Hz for pentas) for the different ℓ modes.

gratings acting as OAM filters displayed by SLM. Lavery *et al.* have demonstrated in the lab that the desired LG mode would expand into its adjacent mode with about 25–35% when there is a lateral displacement of $\Delta x_0 = 0.5w_0$ between the grating and the detection pattern in lab scale [27]. In our experimental setting, a small tilt angle vibration $\Delta\theta$ will cause a magnified displacement $\Delta d = \tan L\Delta\theta \approx L\Delta\theta$ between the detection pattern and the grating, where L is the distance between the sender and receiver. In this case, our detected signal should have an overlap probability:

$$I(t) = \left|\int\int \Phi^*(x,y)\psi(x+\Delta d, y+\Delta d, t)dxdy\right|^2 \propto \left|\sum_\ell \left(B_{\ell',\ell} + B_{-\ell',\ell}\right)\exp(i\ell\Omega t)\right|^2. \quad (3)$$

Note that we describe the beam in Cartesian coordinates here, as this is more convenient in our misalignment considerations. $B_{\ell',\ell} = \sum_{p',p}\int\int[\mathrm{LG}^{\ell'}_{p'}(x,y)]^*\mathrm{LG}^{\ell}_{p}(x,y)\,dxdy$ denotes the total coupling efficiency from the OAM mode ℓ to ℓ' due to the misalignment of the receiver pattern and the grating. If there is no mode spreading, i.e., $B_{\ell',\ell} = \delta_{\ell',\ell}$, we have $I(t) \propto \left|A_{\ell'}\exp(i\ell'\Omega t) + A_{-\ell'}\exp(-i\ell'\Omega t)\right|^2$, which is the trivial case without misalignment. In our experiment, the beam waist w_0 on the grating is about 7.5 mm. As an example simulation to show the mode spreading of the clover and pentas light field, we plot $P'_{\ell'} = \sum_\ell \left|B_{\ell',\ell}\right|^2$ in Figs. 6(a) and 6(b) with $\Delta d = 0.2w_0$, which is corresponding to a small tilt angle vibration $\Delta\theta \approx 0.000013$ rad at the sender. Such tiny swing angles are very likely caused by slight misalignments of the telescope, the SLM or the laser due to mechanical instabilities. To focus on the coupling of the main modes to the contributions of the adjacent ones, we define the spreading ratio as $\xi = (P'_{\mathrm{left}} + P'_{\mathrm{right}})/2P'_{\mathrm{center}}$. One can see [Fig. 6(a)] the dominant modes of $\ell' = \pm 3$ are spreading to the modes $\ell' = \pm 2$ and $\ell' = \pm 4$ with a ratio of nearly 22%. This

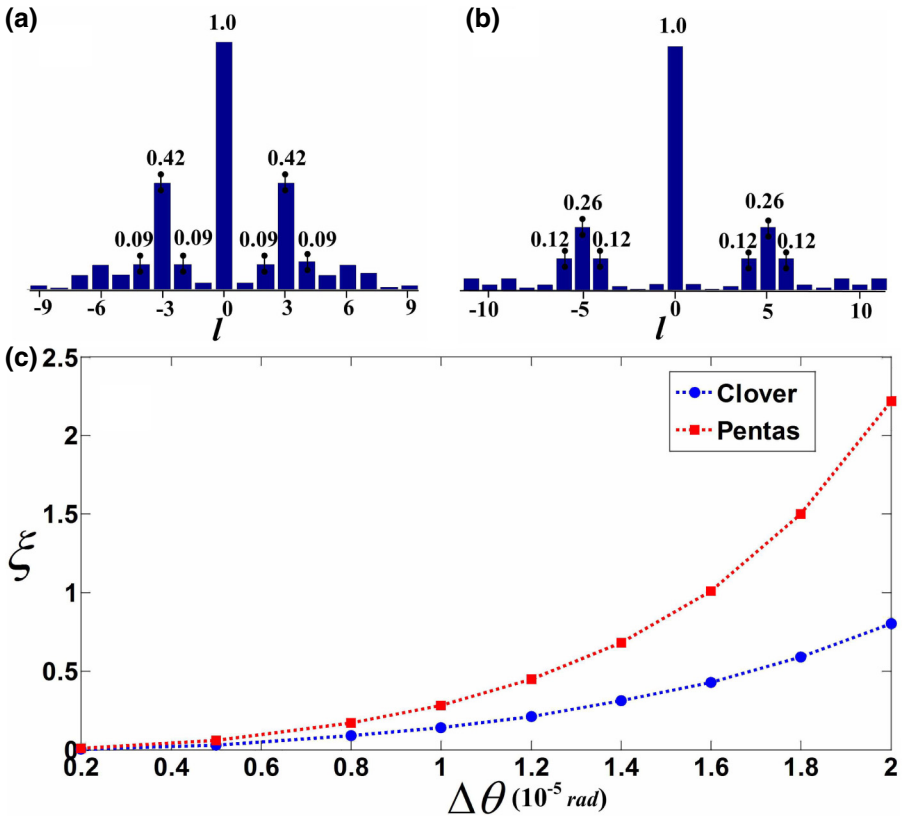

FIG. 6. Influence of the misalignment on the mode spectrum. Simulation results of the mode-spreading effect when there is a small misalignment between the receiver pattern and the grating with $\Delta d = 0.2w_0$ for the (a) clover object, (b) pentas object. (c) The relationship of the spreading ratio and the vibration angle in the sender for both the three-leaf clover object and the five-leaf pentas object. Here the spreading ratio is defined as $\xi_{\text{clover}} = (P'_{|\ell|=2} + P'_{|\ell|=4})/2P'_{|\ell|=3}$ for the clover, while $\xi_{\text{pentas}} = (P'_{|\ell|=4} + P'_{|\ell|=6})/2P'_{|\ell|=5}$ for the pentas.

effect is even stronger for the pentas pattern, where a spreading to the next neighboring modes of up to 46% can be observed [see Fig. 6(b)]. It seems that more complex objects lead to a higher mode-spreading effect. This observation becomes clearer when we plot the spreading ratio with respect to the vibration angle $\Delta\theta$ at the sender [see Fig. 6(c)]. Under the same vibration angle, the five-leaf object always has a higher spreading ratio than the three-leaf object. From this investigation, we see that minimizing vibrations at the sender is crucial, especially when longer measurement times are needed.

Secondly, for a practical free-space optical link, the atmospheric turbulence can lead to random variations in the refractive index such that the phase front of a propagating light is inevitably distorted [28]. This is particularly important for the detection of the rotational Doppler effect, as its measurement is very sensitive to the optical filtering of suitable OAM superposition [11]. Here we adopt the model developed by von Karman to describe the influence of turbulence [29,30] and represent the atmospheric turbulence link as several turbulent phase screens (each averaging 50 phase screens), each separated by some distance of propagation [31,32]. After propagating through the turbulence with a distance Z, the modified light field at the receiver can be written as $\psi'(r, \varphi, Z, t)$. We first perform a numerical simulation with $Z = 120$ m for the clover and pentas image under different air-turbulence strengths C_n^2 in Fig. 7(a). For comparison, we also show the false color image of experimental light field captured at the receiver, as shown in Fig. 7(b). By comparing the simulation results of Fig. 7(a) with the experimental observations of Fig. 7(b), we can conclude that the deformation of the images at the receiver are mainly due to free-space diffraction rather than the air turbulence. So it is reasonable to say that our air-turbulence strength should be on the order of 10^{-15}–10^{-14} $\text{m}^{-2/3}$. To further simulate the effect of atmosphere turbulence on the rotational light field, we use a similar mode-expansion method as described earlier: $A'_{\ell,p} = \int\int [\text{LG}_p^{\ell}(r, \varphi, Z)]^* \psi'(r, \varphi, Z, t) r dr d\varphi$. When taking the atmospheric turbulence effect with a strength such as $C_n^2 = 7.5 \times 10^{-15}$ $\text{m}^{-2/3}$ into account, we only find a very small influence on the pure-OAM spectra characterized by $P'_{\ell} = \sum_p |A'_{\ell,p}|^2$ [see Fig. 7(c)]. For the clover, the power of the dominant single OAM modes, i.e., $\ell' = \pm 3$, is slightly spread to the adjacent modes with around 1 % ratio. For the five-leaf pentas and the dominant modes $\ell' = \pm 5$ to the adjacent modes with around 1.2%.

To identify the turbulence conditions under which the 120-m link might not have worked, we do a further simulation and investigate the relationship between the strength of turbulence (C_n^2) and the mode-spreading ratio (ξ) [see Fig. 7(d)]. It seems that the more complex (pentas) the pattern, the more severe the mode crosstalk. Only strong turbulence in the 120-m link (stronger than 7×10^{-14} $\text{m}^{-2/3}$) will cause $\xi > 100\%$ and may cause the incorrect discrimination of the main mode from the

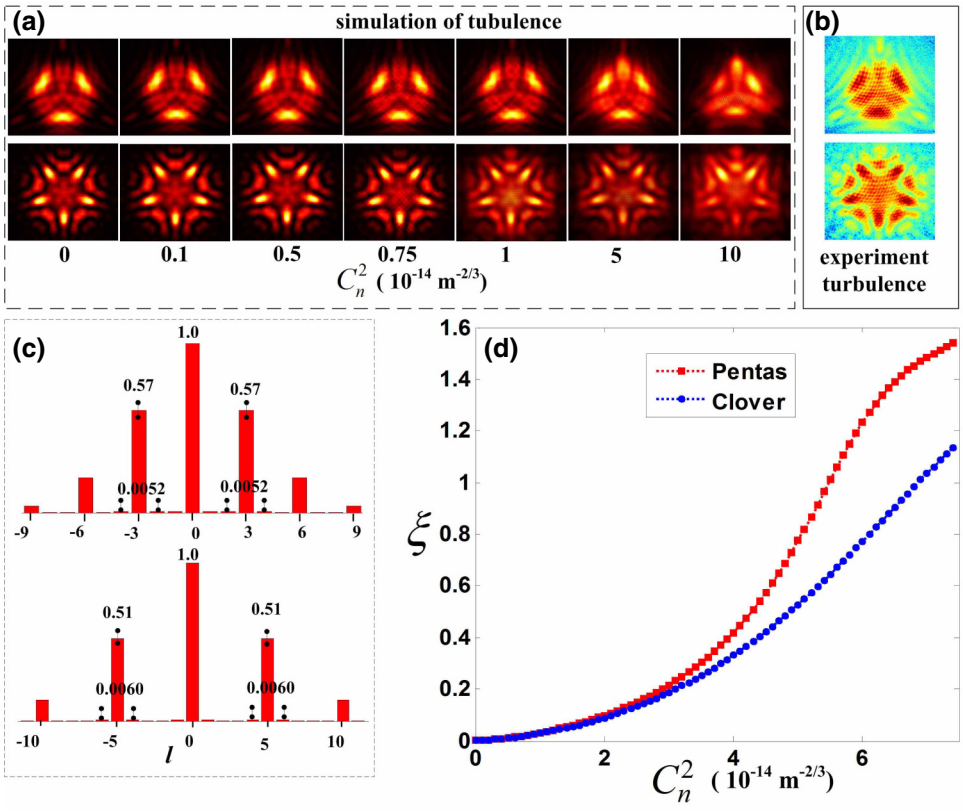

FIG. 7. Influence of the atmospheric turbulence on received patterns. (a) Simulation results of the clover and pentas light fields at the receiver under different turbulence strength. (b) Experimentally obtained results recorded by an EMCCD at the receiver. (c) Simulation results of the slightly disturbed pure-OAM spectra with a turbulence strength of $C_n^2 = 7.5 \times 10^{-15}$ $m^{-2/3}$, which we estimate to resemble our experimental conditions. (d) Simulation results of the variation of the spreading ratio with respect to different turbulence strengths over 120 m.

adjacent one. Thus we conclude that in our situation the atmospheric turbulence only contributed a little to mode-spreading phenomena. On the other hand, except for the vibration angle of the sender, the intensity asymmetry of the light field reflected from the first SLM (due to non-normal incidence) may also cause the modal crosstalk. So it seems that the mode-spreading effect shown by the inset bar graph of Figs. 4 and 5 could be the total effect under our realistic experimental condition.

However, irrespective of where this mode spreading is coming from, misalignment or turbulence, one may always deduce the rotation speed and the rotational symmetry of an unknown rotating object as long as one can clearly discriminate the dominant modes from the spread modes. For longer distance sensing of a rotating object, one will need to address both of the analyzed effects. Here, adaptive optics and machining learning-based pattern recognition may be introduced to compensate the effect of turbulence or misalignment [33].

VI. CONCLUSION

In conclusion, we conduct an outdoor experiment measuring the rotational Doppler effect by building a 120-m free-space optical link in a realistic city environment. Our experimental results with two typical rotating objects, i.e., clover and pentas patterns, demonstrate that long-distance remote sensing of spinning bodies is practically feasible, particularly for those objects possessing a high spatial symmetry. Despite the appearance of frequency shift to adjacent modes that is caused by the slight misalignments and influence of atmospheric turbulence, we can still observe a clearly distinguishable peak of frequency shifts at the desired OAM detection modes, which is associated with the object's rotational symmetry. The effect of the energy spread accompanied with the transfer of frequency shifts from the dominant OAM modes to their adjacent ones was carefully analyzed, which might offer an important value of reference for further exploration of this field. The natural extension of our scheme is to implement the free-space link in a longer distance to detect any rotating bodies [34–36]. Moreover, the ability of our scheme to work at the photon-counting regimes suggests the potential to combine the rotational Doppler effect with a quantum-entangled light source for a long-distance entanglement-enhanced remote-sensing technique [37]. In addition, our feasibility study with extremely low light intensities may pave the way towards applications, such as in covert imaging and biological sensing, where a low-photon flux is essential as a high-photon flux might have detrimental effects [38].

ACKNOWLEDGMENTS

This work is supported by the National Natural Science Foundation of China (NSFC) (Grants No. 11474238 and No. 91636109), the Fundamental Research Funds

for the Central Universities at Xiamen University (Grant No. 20720160040), the Natural Science Foundation of Fujian Province of China for Distinguished Young Scientists (Grant No. 2015J06002), and the program for New Century Excellent Talents in University of China (Grant No. NCET-13-0495). R.F. is grateful for financial support from the Banting postdoctoral fellowship of the Natural Sciences and Engineering Research Council of Canada (NSERC).

[1] R. M. Measures, *Laser Remote Sensing, Fundamentals and Applications* (John Wiley and Sons, New York, 1984).
[2] M. Padgett, Electromagnetism: Like a speeding watch, Nature **443**, 924 (2006).
[3] B. A. Garetz, and S. Arnold, Variable frequency shifting of circularly polarized laser radiation via a rotating half-wave retardation plate, Opt. Commu. **31**, 1 (1979).
[4] R. Simon, H. J. Kimble, and E. C. G. Sudarshan, Evolving Geometric Phase and its Dynamical Manifestation as a Frequency Shift: An Optical Experiment, Phys. Rev. Lett. **61**, 19 (1988).
[5] G. Li, Z. Thomas, and S. Zhang, Rotational doppler effect in nonlinear optics, Nat. Phys. **12**, 736 (2016).
[6] L. Allen, M. W. Beijersbergen, R. J. C. Spreeuw, and J. P. Woerdman, Orbital angular momentum of light and the transformation of Laguerre-Gaussian laser modes, Phys. Rev. A **45**, 8185 (1992).
[7] J. Courtial, K. Dholakia, D. A. Robertson, L. Allen, and M. J. Padgett, Measurement of the Rotational Frequency Shift Imparted to a Rotating Light Beam Possessing Orbital Angular Momentum, Phys. Rev. Lett. **80**, 3217 (1998).
[8] J. Courtial, D. A. Robertson, K. Dholakia, L. Allen, and M. J. Padgett, Rotational Frequency Shift of a Light Beam, Phys. Rev. Lett. **81**, 4828 (1998).
[9] S. Barreiro, J. W. R. Tabosa, H. Failache, and A. Lezama, Spectroscopic Observation of the Rotational Doppler Effect, Phys. Rev. Lett. **97**, 113601 (2006).
[10] O. Korech, U. Steinitz, R. J. Gordon, I. S. Averbukh, and Y. Prior, Observing molecular spinning via the rotational Doppler effect, Nat. Photon. **7**, 711 (2013).
[11] M. P. Lavery, F. C. Speirits, S. M. Barnett, and M. J. Padgett, Detection of a spinning object using lights orbital angular momentum, Science **341**, 537 (2013).
[12] M. P. Lavery, S. M. Barnett, F. C. Speirits, and M. J. Padgett, Observation of the rotational Doppler shift of a white-light, orbital-angular-momentum-carrying beam backscattered from a rotating body, Optica **1**, 1 (2014).
[13] C. Rosales-Guzmn, N. Hermosa, A. Belmonte, and J. P. Torres, Measuring the translational and rotational velocities of particles in helical motion using structured light, Opt. Express **22**, 16504 (2014).
[14] L. Fang, M. Padgett, and J. Wang, Sharing a common origin between the rotational and linear Doppler effects, Laser Photon. Rev. **11**, 1770064 (2017).
[15] M. Zhao, X. Gao, M. Xie, W. Zhai, W. Xu, S. Huang, and W. Gu, Measurement of the rotational Doppler frequency shift of a spinning object using a radio frequency orbital angular momentum beam, Opt. Lett. **41**, 2549 (2016).
[16] H. Zhou, D. Fu, J. Dong, P. Zhang, D. Chen, X. Cai, F. Li, and X. Zhang, Orbital angular momentum complex spectrum analyzer for vortex light based on the rotational Doppler effect, Light Sci. Appl. **6**, e16251 (2017).
[17] M. Padgett, A new twist on the Doppler shift, Phys. Today **67**, 58 (2014).
[18] L. Marrucci, Spinning the Doppler effect, Science **341**, 464 (2013).
[19] A. E. Willner *et al.*, Optical communications using orbital angular momentum beams, Adv. Opt. Photon. **7**, 66 (2015).
[20] L. Torner, J. P. Torres, and S. Carrasco, Digital spiral imaging, Opt. Express **13**, 873 (2005).
[21] D. Petrov, N. Rahuel, G. Molina-Terriza, and L. Torner, Characterization of dielectric spheres by spiral imaging, Opt. Lett. **37**, 869 (2012).
[22] L. Chen, J. Lei, and J. Romero, Quantum digital spiral imaging, Light Sci. Appl. **3**, e153 (2014).
[23] W. Zhang, and L. Chen, Encoding and decoding of digital spiral imaging based on bidirectional transformation of light's spatial eigenmodes, Opt. Lett. **41**, 2843 (2016).
[24] W. Zhang, Z. Wu, J. Wang, and L. Chen, Experimental demonstration of twisted lights diffraction theory based on digital spiral imaging, Chin. Opt. Lett. **14**, 110501 (2016).
[25] M. Vasnetsov, V. Pas'Ko, and M. Soskin, Analysis of orbital angular momentum of a misaligned optical beam, New J. Phys. **7**, 46 (2005).
[26] M. Lavery, K. Peuntinger, C. Günthner, P. Banzer, D. Elser, R. W. Boyd, M. Padgett, C. Marquardt, and G. Leuchs, Free-space propagation of high-dimensional structured optical fields in an urban environment, Sci. Adv. **3**, e1700552 (2017).
[27] M. Lavery, G. Berkhout, J. Courtial, and M. Padgett, Measurement of the light orbital angular momentum spectrum using an optical geometric transformation, J. Opt. **13**, 064006 (2011).
[28] C. Paterson, Atmospheric Turbulence and Orbital Angular Momentum of Single Photons for Optical Communication, Phys. Rev. Lett. **94**, 153901 (2005).
[29] R. G. Lane, A. Glindemann, and J. C. Dainty, Simulation of a Kolmogorov phase screen, Waves Random Media **2**, 209 (1992).
[30] V. E. Ostashev, B. Brähler, V. Mellert, and G. H. Goedecke, Coherence functions of plane and spherical waves in a turbulent medium with the von Karman spectrum of medium inhomogeneities, J. Acoust. Soc. Am. **104**, 727 (1998).
[31] S. Fu, and C. Gao, Influences of atmospheric turbulence effects on the orbital angular momentum spectra of vortex beams, Photon. Res. **4**, B1 (2016).
[32] S. Zhao, J. Leach, L. Gong, J. Ding, and B. Zheng, Aberration corrections for free-space optical communications in atmosphere turbulence using orbital angular momentum states, Opt. Express **20**, 452 (2012).
[33] Y. Ren *et al.*, Adaptive-optics-based simultaneous pre-and post-turbulence compensation of multiple orbital-angular-momentum beams in a bidirectional free-space optical link, Optica **1**, 376 (2014).

[34] M. Krenn, R. Fickler, M. Fink, J. Handsteiner, M. Malik, T. Scheidl, R. Ursin, and A. Zeilinger, Communication with spatially modulated light through turbulent air across Vienna, New J. Phys. **16**, 113028 (2014).

[35] M. Krenn, J. Handsteiner, M. Fink, R. Fickler, R. Ursin, M. Malik, and A. Zeilinger, Twisted light transmission over 143 km, Proc. Natl. Acad. Sci. **113**, 13648 (2016).

[36] F. Tamburini, B. Thid, G. Molina-Terriza, and G. Anzolin, Twisting of light around rotating black holes, Nat. Phy. **7**, 195 (2011).

[37] M. Krenn, J. Handsteiner, M. Fink, R. Fickler, and A. Zeilinger, Twisted photon entanglement through turbulent air across vienna, Proc. Natl. Acad. Sci. **112**, 14197 (2015).

[38] P. Morris, R. Aspden, J. E. Bell, R. W. Boyd, and M. Padgett, Imaging with a small number of photons, Nat. Commun. **6**, 5913 (2015).